Proton-Driven Dynamic Behavior of Nanoconfined Water in Hydrophilic MXene Sheets

Pengfei Hou,[a,b] Yumiao Tian,[a,b] Yu Xie,[a,b] Quan Li,[b,c] Gang Chen,[a] Fei Du,*[a] Jianzhong Wu,*[d] Yanming Ma,[b,c,e] Xing Meng,*[a,b]

[a] P. Hou, Y. Tian, Prof. Y. Xie, Prof. G. Chen, Prof. F. Du, Dr. X. Meng, Key Laboratory of Physics and Technology for Advanced Batteries (Ministry of Education), College of Physics, Jilin University, Changchun 130012, P. R. China
E-mail: mengxing@jlu.edu.cn (Xing Meng); dufei@jlu.edu.cn (Fei Du)
[b] P. Hou, Y. Tian, Prof. Y. Xie, Prof. Q. Li, Prof. Y. Ma, Dr. X. Meng, Key Laboratory of Material Simulation Methods and Software of Ministry of Education, College of Physics, Jilin University, Changchun 130012, China
E-mail: mengxing@jlu.edu.cn (Xing Meng)
[c] Prof. Q. Li, Prof. Y. Ma, International Center of Future Science, Jilin University, Changchun 130012, China
[d] Prof. J. Wu, Department of Chemical and Environmental Engineering, University of California, Riverside, California 92521, USA
E-mail: jwu@engr.ucr.edu (Jianzhong Wu)
[e] Prof. Y. Ma, State Key Laboratory of Superhard Materials, College of Physics, Jilin University, Changchun 130012, China

Supporting information for this article is given via a link at the end of the document.

Abstract: Liquid water under nanoscale confinement has attracted intensive attention due to its pivotal role in understanding various phenomena across many scientific fields. MXenes serve an ideal paradigm for investigating the dynamic behaviors of nanoconfined water in a hydrophilic environment. Combining deep neural networks and an active learning scheme, here we elucidate the proton-driven dynamics of water molecules confined between V_2CT_x sheets using molecular dynamics simulation. Firstly, we have found that the Eigen and Zundel cations can inhibit water-induced oxidation by adjusting the orientation of water molecules, thus proposing a general antioxidant strategy. Besides, we also identified a hexagonal ice phase with abnormal bonding rules at room temperature, rather than only at ultralow temperatures as other studies reported, and further captured the proton-induced water phase transition. This highlighted the importance of protons in the maintaining stable crystal phase and phase transition of water. Furthermore, we discussed the conversions of different water structures and water diffusivity with changing proton concentrations in detail. The results provide useful guidance in practical applications of MXenes including developing antioxidant strategies, identifying novel 2D water phases and optimizing energy storage and conversion.

Introduction

Liquid water in low-dimensional systems exhibit unique properties that have attracted broad scientific interests for their potential applications in various fields including materials science [1], cell biology [2], and condensed matter physics [3]. The nanoconfinement can significantly alter the dynamic behaviors of water molecule and promote distinctive structure arrangements unseen in bulk systems. For example, both theoretical calculations [4] and experiments [5] have demonstrated that nanoconfined water is able to form two-dimensional ice with hexagonal, pentagonal, square and many other structures that have different rules of hydrogen bonding compared to the bulk ice. In addition, nanoconfined water often shows abnormal physicochemical properties, such as ultralow dielectric constant [3b] and high proton conduction [3d], and may exist in a superionic state [4c]. Advanced understanding of nanoconfined water will facilitate progress across many scientific disciplines, enabling exploration of novel physicochemical mechanisms and broadening the boundaries of science.

Among various two-dimensional (2D) materials containing nanoconfined water, transition metal carbides/nitrides [6], known as MXenes, offer an ideal paradigm for investigating the distinctive properties of nanoconfined water at hydrophilic interfaces. MXenes are a large family of 2D materials with the chemical formula of $M_{n+1}X_nT_x$, where M stands for early transition metals, X for C/N, T_x for -O, -OH or other groups, and n=1, 2, 3 or 4 represents the number of C/N layers. [7] The -O/-OH groups on MXene surface result in super hydrophilicity. [8] Nanoconfined water in MXene sheets is intricately linked to many practical applications. [9] For example, the polarization of nanoconfined water within 2D titanium carbide sheets can enhance the capacitance of electric double-layer capacitors. [10] Our previous research reveals that the MXene oxidation rate decreases with the increase of the nanoconfined water layer thickness. [11]

In addition, protons are widely present in MXene systems. The proton redox process (-O and -OH convert to each other) and the transport mechanism of hydrated protons play a crucial role in energy-related applications. [12] The proton-dependent process also complicates the dynamic behavior of nanoconfined water in MXenes. For example, Petit et al. [12b] observed discrete vibration patterns arising from the reduced coordination number of protons in nanoconfined water through operando infrared spectroscopy, which suggested that protons could dramatically modulate the nanoconfined water molecules. An in-depth study of nanoconfined water in MXene systems could not only guide their practical applications in various fields but also facilitate the understanding of nanoconfined water, especially at hydrophilic interfaces.

In this work, we develop a deep neural network potential (NNP) for nanoconfined water in vanadium carbide MXene with mixed -O/-OH terminal groups and different proton contents. Utilizing the

NNP, we unveiled the intricate proton-driven dynamic behaviors of large-scale monolayer nanoconfined water within hydrophilic MXene sheets. These findings have illuminated several novel phenomena including the MXene oxidation rate regulated by hydrated protons, the formation of a hexagonal ice phase exhibiting unconventional bonding patterns at room temperature, and a significant reduction in water diffusivity, which can largely be attributed to the proton effect and the MXene hydrophilic surface.

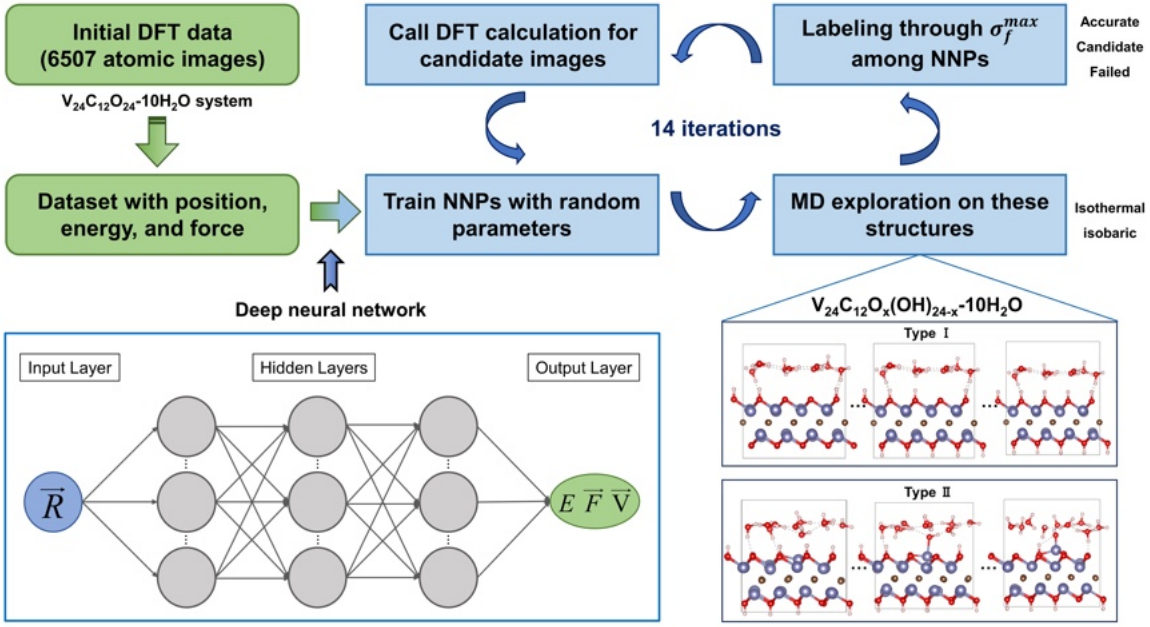

Figure 1. The flowchart in developing the NNP for V_2CT_x-H_2O-H systems with the active learning approach.

Results and Discussion

NNP training. Our NNP is constructed by using the Deep potential scheme [13] that incorporates active learning methods. As shown in Figure 1, the flowchart starts with 6507 initial DFT data for the monolayer nanoconfined water in V_2CO_2 interlamination ($V_{24}C_{12}O_{24}$-10H_2O systems) reported in our previous work. [11] The dataset includes information about atomic positions, potential energies, and atomic forces. An iterative active learning process is carried out utilizing the deep neural network algorithm. The whole process could be divided into four stages: training, exploration, labeling, and correction. In the training stage, different NNPs are trained with diverse random parameters. Next, we perform molecular dynamics (MD) simulation in the isothermal-isobaric (NPT) ensemble to explore the nanoconfined water within V_2CT_x sheets at different proton concentrations ($V_{24}C_{12}O_x(OH)_{24-x}-10H_2O$ systems). During the labeling stage, we evaluate the deviations of different NNPs according to the maximal atomic force deviation (σ_f^{max}) and label the MD snapshots as accurate, candidate or failed based on $\sigma_f^{max} < \sigma_l$, $\sigma_l \leq \sigma_f^{max} < \sigma_h$, or $\sigma_f^{max} \geq \sigma_h$, where σ_l and σ_h correspond to the lowest and highest trust levels, respectively. In the correction stage, we calibrate the NNPs by adding the DFT results from the candidate snapshots into dataset. The iterative active learning process concludes once almost all snapshots are labeled as accurate. A high-quality NNP was obtained by using 29823 pieces of DFT data collected from 98.78 million snapshots after 14 iterations. The final NNP achieves a root-mean-square error of 1.39 meV/atom for energy and 83 meV/Å for force on the test dataset. The detailed training process, NNP accuracy testing, and parameter settings are listed in Supporting Information.

Leveraging the NNP, we performed large-scale MD simulations to investigate the dynamic behaviors of nanoconfined water in V_2CT_x sheets (~10 nm in thickness containing 1000 H_2O molecules) under different proton concentrations. Specifically, NPT MD simulations were conducted for 12 systems with the initial proton concentration at 0% H, 1% H, 3% H, 5% H, 10% H, 15% H, 20% H, 25% H, 30% H, 40% H, 50% H, and 80% H (versus H_2O molecules). For all systems, considering the actual MXene surface with mixed O/-OH, [14] the corresponding protons are randomly added to the -O groups on the V_2CT_x surface at the initial condition.

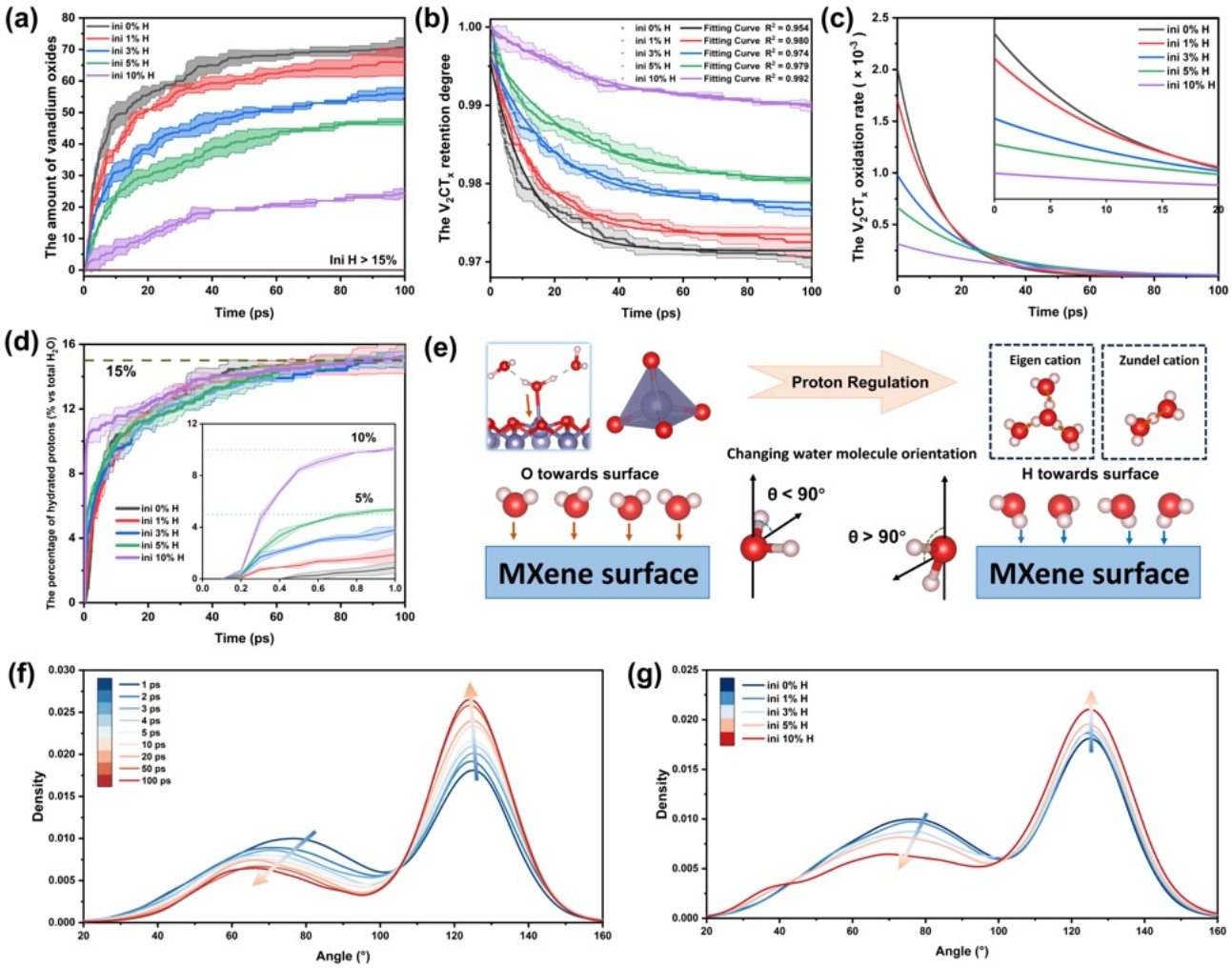

Figure 2. The kinetics of MXene oxidation. (a) The variation of the amount of vanadium oxides on the V_2CT_x surface with simulation time. (b) The degree of V_2CT_x retention versus simulation time. The solid lines are the corresponding exponential fitting results using the double exponential function. (c) The oxidation rate of the V_2CT_x sheets versus the simulation time, from the fitting results using the double exponential function. (d) The variation of the percentage of hydrated protons in water with simulation time. (e) Schematic diagram of the proton regulation on V_2CT_x oxidation. (f) The probability distribution of the angle θ for the 0% H system at different simulation durations (from 0 ps to 100 ps). (g) The probability distribution of the angle θ at 1 ps for initial 0% H, 1% H, 3% H, 5% H and 10% H systems. The amount of vanadium oxides, the V_2CT_x retention degree, and the percentage of hydrated protons all take the average value from three independent simulations (n = 3) and the pale shade represents the error bars that stand for the standard deviation of the results. The exponential fits are obtained from the average V_2CT_x retention degree and the fitted parameters and the determination coefficient R^2 are shown in the Table S1 in Supporting Information. Figure 2f and Figure 2g are obtained by the kernel density estimate methods through counting the angle θ of each water molecule in three independent simulations at the corresponding times and systems.

The MXene oxidation rate regulated by protons. As shown in Figure 2a and 2b, the statistical amount of vanadium oxides and the degree of V_2CT_x retention (i.e., the unoxidized V_2CT_x area) follow the exponential rule with time. We found a significant reduction of the oxidation rate when the initial proton concentration increases from 0% H to 10% H, indicating that the oxidation reaction is regulated by protons. Particularly noteworthy is the absence of the observable oxides on the surface in systems with more than 15% H, as shown in the brown horizontal line of Figure 2a. The subsequent discussion related to the oxidation will be carried out in the systems with initial proton contents from 0% H to 10% H.

Further, we performed the fitting on the relationship between the retention degree of V_2CT_x sheets and the simulation time by following the double exponential decay function:

$$\alpha(t) = A_1 e^{-t/t_1} + A_2 e^{-t/t_2} \quad (1)$$

where $\alpha(t)$ represents the retention degree of V_2CT_x sheets, A_1, A_2, t_1, t_2 are parameters to be fitted, and t and e are the simulation time and the natural constant respectively. The fitting parameters and determination coefficient R^2 are shown in the Table S1, and all the R^2 are greater than 0.95, showing that the function can well reflect our simulation results. From results shown in Table S1, we can see that the t_2 parameters are extremely large (> 10^{26}), suggesting that this parameter only

works after a long enough simulation time. As the simulation time approaches infinity, the retention degree of V_2CT_x sheets is close to 0. This is consistent with the experimental observation that MXenes are fully oxidized over a duration ranging from a few weeks to several months, rather than in hundreds of picoseconds. That is why we originally chose the double exponential function. But in analyzing the results from simulations of the hundreds of picoseconds subsequently, the second term on the right side of Eq. (1) can be treated as a constant $A_0 = A_2 e^{-t/t_2} \approx A_2$. Hence the Eq. (1) is simplified as the single exponential function:

$$\alpha(t) = A_0 + A_1 e^{-t/t_1} \quad (2)$$

which indicates the oxidation kinetics of V_2CT_x is similar to the first-order reaction. Then we can calculate the oxidation degree of V_2CT_x from:

$$1 - \alpha(t) = 1 - A_0 - A_1 e^{-t/t_1} \quad (3)$$

Accordingly, the oxidation rate of V_2CT_x, $k(t)$, can be obtained as follow:

$$k(t) = \frac{\mathrm{d}(1-\alpha(t))}{dt} = -\frac{\mathrm{d}(\alpha(t))}{dt} = \frac{A_1}{t_1} e^{-t/t_1} = k_0 A_1 e^{-t/t_1} \quad (4)$$

where k_0 stand for the time-independent rate constants of the first-order reaction. The rate constants of the systems initially with 0% H, 1% H, 3% H, 5% H, and 10% H are shown in Figure S4. As the initial proton contents increase, the rate constants decrease monotonously, indicating the significant role of protons in inhibiting oxidation of MXenes. Figure 2c represents the relationship of the oxidation rates and the simulation time for different systems. The oxidation rate of V_2CT_x decays exponentially with simulation time for all systems. The exponential decay results from the increasing hydrated protons due to the oxidation reaction. At the early stage, the oxidation rate significantly decreases as the initial proton concentration increases, indicating the significant role of hydrated protons in inhibiting oxidation of MXenes. With the simulation time increases, the oxidation rate decreases rapidly with the simulation time and eventually reach a similar value when all systems have similar hydrated proton concentrations (Figure 2d). In 1% H, 3% H, 5% H, and 10% H systems, the hydrated protons sharply increase within the initial 1 ps (the embedded figure in Figure 2d) because of the rapid cleavage of the -OH groups (Figure S5) on the MXene surface. After that, the hydrated protons continue to increase with time because of the proton release in the oxidation reaction. Considering the inhibition of the hydrated protons on the oxidation rate, the systems with a low initial proton concentration (such as 0% H, 1% H, and 3% H) will undergo rapid oxidation reaction, resulting in a quick increase in the number of hydrated protons, whereas systems with a higher initial concentration of protons (5% H and 10% H) have a relatively slower rate in generating hydrated protons due to the lower oxidation rates. At the late period of the simulation, the concentrations of hydrated protons converge to a similar value for all systems and the oxidation rate becomes basically the same. Further the relationship between the oxidation rate and the hydrated proton concentration is given in the Figure S6. The oxidation rate of all systems decreases with increasing hydrated protons, again emphasizing the significant proton effect on oxidation rate of MXenes.

Besides, we also selected the single exponential function, $\alpha(t) = A_0 + A_1 e^{-t/t_1}$, as the initial fitting function and performed the same kinetics analysis. The relevant results are shown in Table S2 and Figure S7. These results are in good agreement with the previous results from the double exponential functions, proving the robustness of the above conclusions.

To elucidate the underlying mechanism of MXene oxidation regulated by hydrated protons, we first consider the differences in the orientations of water molecules between those involved in the oxidation reaction and those in the hydrated protons. For the oxidation reaction, the critical step is H_2O adsorption (Figure 2e), in which the oxygen atoms of the water molecules attach to the MXene surface. While for solvated hydrated protons, whether in the Zundel-type or in the Eigen-type structure, the oxygen atoms in the surrounding water molecules are always located near the proton at the center. The water molecules in these two situations are mutually exclusive. Once the proton is hydrated, the water molecules in the solvation structure will not participate in the oxidation reaction. Based on the above analysis, we deduced that the hydrated protons could essentially inhibit the MXene oxidation through reducing the amount of water molecules involved in the oxidation reaction.

To validate the conjecture, we constructed an angle descriptor θ, which is defined as the angle of the bisector of each H_2O molecule and the basal normal, to describe the water orientation with respect to MXene surface. When the O atoms of water molecules are attached to the MXene surface with an acute angle, $\theta < 90°$. By contrast, for water molecules associated with the hydrated protons, the H atoms tend to contact with the MXene surface, leading to $\theta > 90°$. In this case, their O atoms have been captured by the central proton and no longer directly interact with the MXene surface. We first considered 0% H system to validate the conjecture because its hydrated protons can increase from 0 % to about 15% as well as the oxidation rate decreases monotonically (Figure S6). Figure 2f presents the probability distribution of the angle θ at different durations in the 0% H system. It can be seen that, as time progresses up to 100 ps, the probability distribution for $\theta < 90°$ gradually decreases, while that for $\theta > 90°$ increases. This shift indicates that the increasing hydrated protons results in the transformation in the water orientation from the O atom adsorption to the H atom adsorption on the MXene surface and the decrease in the amount of water molecules involved in the oxidation reaction, thus reducing the oxidation rate.

To further prove the reliability of our simulation results, we analyzed the probability distribution of the angle θ for systems initially with 0% H, 1% H, 3% H, 5% H, and 10% H at 1 ps. As shown in Figure 2g, the probability density decreases for $\theta < 90°$ and increases for $\theta > 90°$ as the initial proton concentration increases from 0% H to 10% H. Meanwhile, the oxidation rate of these systems decreases (Figure 2c) at 1ps. These observations provide compelling evidence that hydrated protons indeed modulate the oxidation rate through regulating the orientation of water molecules relative to the MXene surface.

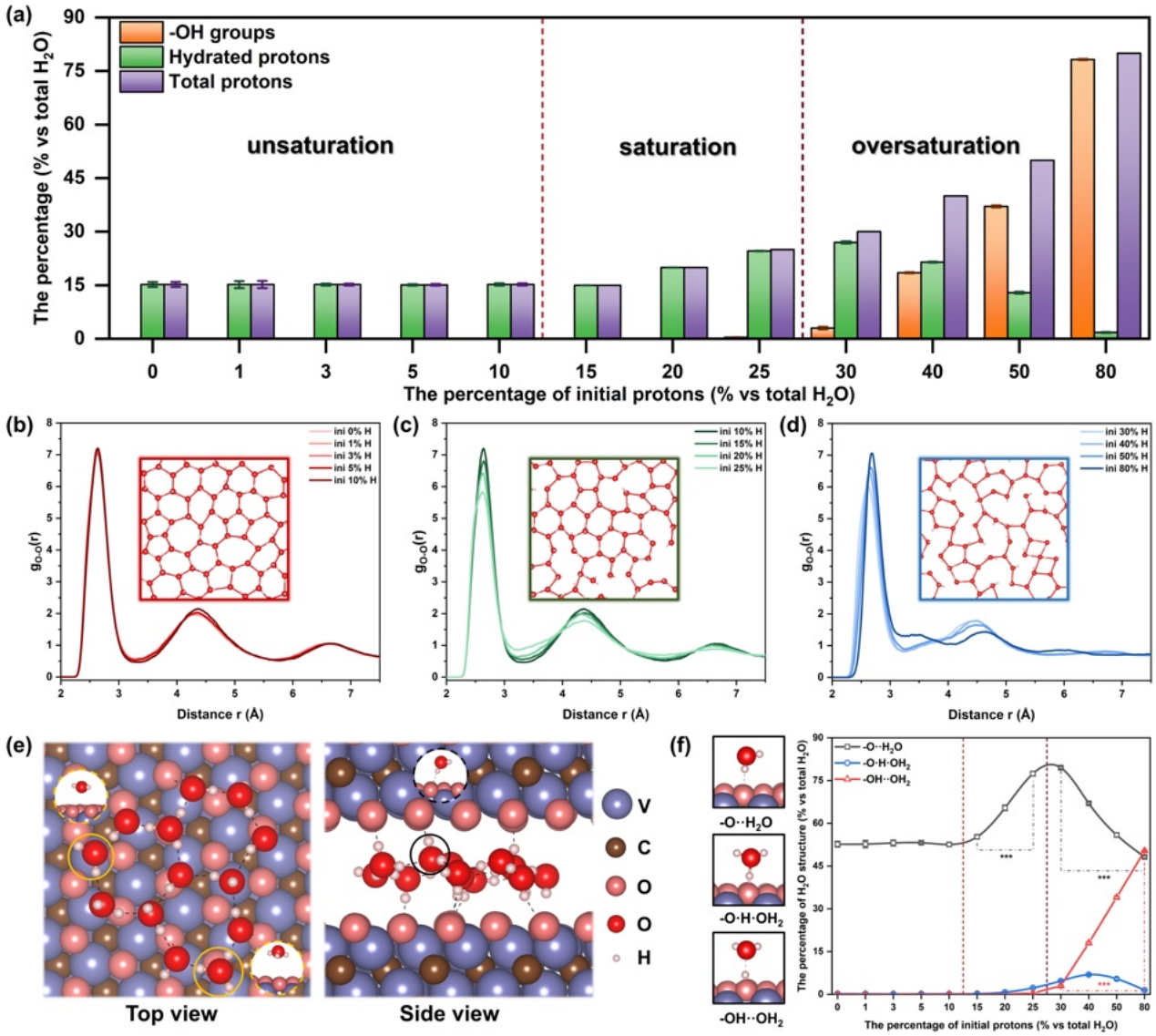

Figure 3. The evolution of protons, a hexagonal ice phase and water structures. (a) The existence forms and percentage of protons in the V_2CT_x systems containing different initial proton concentrations (from 0% H to 80% H). The oxygen-oxygen pair distribution functions and the lateral water structure in unsaturation (b), saturation (c), and oversaturation (d) systems. Other $g_{O\text{-}O}(r)$ from the independent MD simulations are shown in Figure S8. (e) The top and side views of 2D hexagonal ice between V_2CT_x sheets. (f) The percentage of different types of water structures as the initial proton concentration increases. The percentage of hydroxyl groups, hydrated protons, and water structures all take the average value from three independent MD simulations, and each MD simulation takes into account the average value at the last 1ps. The error bars are shown in the relevant region and stand for the standard deviation of the results. Statistical analysis, *p < 0.05, **p < 0.01, ***p < 0.001.

Hexagonal ice between hydrophilic MXene sheets. For the sake of clarity in further discussion, we divide the twelve systems (from 0% H to 80% H) into three groups based on the forms of proton existence: unsaturation, saturation, and oversaturation (Figure 3a). In the unsaturation systems, there exists no -OH groups, and the final hydrated proton concentrations are almost the same for the systems ranging from 0% to 10% H, indicating that the excess protons come from the oxidation reaction. In the saturation systems (15%-25% H), there is no oxidation occurring, and all protons exist in the form of hydrated protons. In the oversaturation systems (30%-80% H), the surface -OH groups rise with the increasing initial proton concentration. The disparate forms of proton existence may lead to different distributions of water molecules in these systems.

To further illustrate the distribution patterns of the monolayer water, Figure 3b-3d present the oxygen-oxygen pair distribution functions, $g_{o\text{-}o}(r)$, for all 12 systems. For the unsaturation systems, two distinct peaks are observed in the $g_{o\text{-}o}(r)$, signifying the presence of first- and second-nearest neighbors of O atoms in the hexagonal ice phase (Figure 3b). Similar phase have been identified in other nanoconfined water systems at ultralow temperature, such as about 120 K for Au(111)/Pt(111) surfaces [1a, 5a] and below 200 K in graphene [4b, 4c]. The unsaturation systems display similar $g_{o\text{-}o}(r)$ profiles due to the uniform final

hydrated proton concentration in these systems. As the proton concentration increases, the hexagonal ice phase gradually disappears, although major six-membered ring structures persist (Figure 3c). In the oversaturation systems (Figure 3d), the second peak of the $g_{o\text{-}o}(r)$ vanishes along with the complete disruption of the 2D hexagonal ice phase.

Figure 3e represents the top and side views of the leaving three six-membered rings after removing the excess water molecules from the whole hexagonal ice phase (Figure 3b). It is evident that the ordered six-membered rings are composed of water molecules or hydrated protons, with the water molecules oriented vertically or parallelly to the MXene surface. The formation of six-membered rings is attributed to the synergistic effect of the in-plane hydrogen bonds among water molecules and the surface hydrogen bonds between water molecules and the MXene surface. In particular, the unique surface hydrogen bonds in the hydrophilic systems restrict the movement of water molecules and thus sustain the hexagonal ice phase. This phenomenon elucidates why the hexagonal ice could be observed in MXene sheets at room temperature, rather than ultralow temperatures. In addition, the hydrated protons present in the six-membered ring act as a lubricant and help mitigate the vigorous movement of water molecules, thereby preserving the six-membered ring configuration. These results indicate that the formation mechanism of the hexagonal ice phase for the monolayer water in hydrophilic MXene sheets is completely different from that of the common hexagonal ice phase in other water systems.

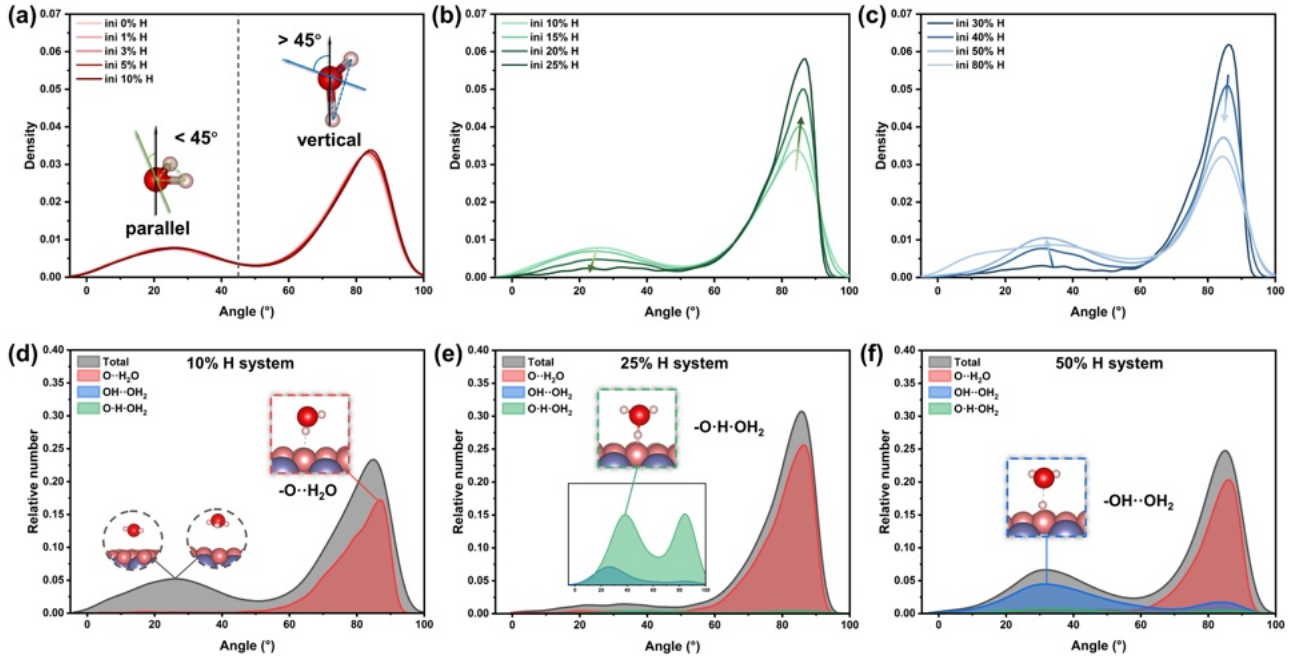

Figure 4. Spatial orientation of water structures. The density distributions of nanoconfined water with angle φ for (a) unsaturation systems, (b) saturation systems, and (c) oversaturation systems. The relative number of different water structures in the systems with initial (d) 10% H, (e) 25% H, and (f) 50% H. Figure 4a-4f are obtained by counting the angle φ of each water molecule for systems with different initial proton contents in the last 1ps of three independent MD simulations and then acquired the angle φ distribution using the kernel methods. The relative number of different water structures in 10% H, 25%H, 50% H systems are shown here. See Figure S9 for that for other systems.

Spatial orientation of water structures. Given that the presence of the hexagonal ice phase relies on the surface hydrogen bonds, the disappearance of this phase in the saturation and oversaturation systems likely indicates the changes in the interaction between water molecule and MXene surface. In fact, we may identify three structures according to the relationship between MXene surface and water molecules, namely -O··H_2O, -OH··OH_2, and -O·H·OH_2 (Figure 3f). Only -O··H_2O structure exists in the unsaturation systems, and the percentages are largely consistent across different proton concentrations. For the saturation systems, increasing the proton concentration results in a higher percentage of -O··H_2O structure, indicating a stronger hydrogen bond interaction between the water layer and the MXene surface. It is worth noting that the -O·H·OH_2 structures gradually emerge during this stage, serving as the transition state for the transformation of the hydrated proton to the -OH groups. With the further increase of proton concentrations, many hydrated protons transform into -OH groups in the oversaturation systems. Consequently, we observe a decrease of -O··H_2O structures and an increase in -OH··OH_2 structures. The transition among the three H_2O structures reflects the evolving interactions between water molecule and MXene surface, which is an important factor contributing to the disappearance of the hexagonal ice phase.

Then the distribution of water molecules is investigated through constructing another angle descriptor, denoted as φ, which is defined by the angle between the H-O-H plane normal of H_2O and the basal normal. Water molecules tend to align vertically and parallel to the MXene surface when φ is greater and less than 45°. Figure 4 presents the density distributions of nanoconfined water with angle φ under different proton concentrations and the relative number of different water

structures, which can stand for spatial orientation of water molecules. The density distributions are virtually identical for the unsaturation systems (Figure 4a), characterized by abundant -O··H_2O structures vertical to the surface and a moderate amount of water molecules or hydrated protons parallel to the surface (Figure 4d). The result is consistent with previous observation from the top and side view of the hexagonal ice phase. For the saturation systems, as the proton concentration increases, the part of the curve less than 45° decreases while that greater than 45°increases (Figure 4b). This trend indicates a shift in the majority of water molecules from a parallel to a vertical orientation with respect to the surface, ultimately leading to the destruction of the hexagonal ice phase. The transition structures (-O·H·OH_2) begin to emerge and gradually rise during this stage as shown in Figure 4e. In the oversaturation systems, the portion of the curve less than 45° increases while that greater than 45° decreases (Figure 4c). Although the shape of the curve is identical to that of the unsaturation systems, the portion of the curve less than 45° for the oversaturation systems is mainly contributed by water molecules that strongly hydrogen bonding to -OH groups on the MXene surface (Figure 4f). The above results reveal that the spatial orientation of the monolayer nanoconfined water with respect to the MXene surface could be achieved by adjusting the proton concentration. The proton modulation elucidates the fundamental reason for the appearance and disappearance of the hexagonal ice phase.

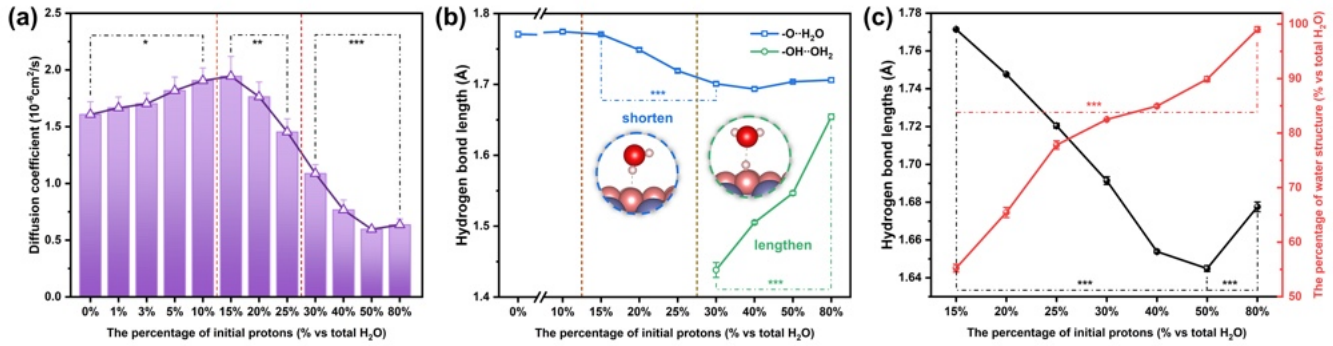

Figure 5. Diffusivity and hydrogen bond lengths of nanoconfined water. (a) The oxygen diffusion coefficients at different proton concentrations. (b) The surface hydrogen bond lengths in the -O··H_2O and -OH··OH_2 structure, respectively, at different proton concentrations. (c) The percentage of -O··H_2O and -OH··OH_2 structures and their average surface hydrogen bond lengths at different proton concentrations. The oxygen diffusion coefficients are obtained by linearly fitting between 20 ps and 60 ps for the mean square displacement (MSD) using the Einstein relation in three independent simulations (n = 3). The relevant MSD are shown in Figure S10 and the determination coefficients R^2 of the fitting results are all greater than 0.99. Figure 5b and Figure 5c all take the average value from three independent MD simulations (n = 3), and each MD simulation takes into account the average values at the last 1ps. The error bars are shown in the relevant region and stand for the standard deviation of the results. Statistical analysis, *p < 0.05, **p < 0.01, ***p < 0.001.

Diffusivity of nanoconfined water. Figure 5a illustrates the oxygen diffusion coefficient of nanoconfined water under different proton concentrations. For the unsaturation systems, the oxygen diffusion coefficient increases gradually with the initial proton concentration. The rising diffusion coefficient in the unsaturation systems is attributed to the inhibited water-induced oxidation reaction with the increasing proton concentrations. The oxide formation requires the participation of plentiful water molecules that are confined to a small region during the oxidation process, thus reducing the mobility of the water molecules.

Conversely, the diffusion coefficient falls rapidly with the proton concentration in the saturation and oversaturation systems, which is closely related to the water structures, -O··H_2O structure and -OH··OH_2 structure. For the saturation systems, the decreasing diffusion coefficient with rising proton concentration is attributed to by the increasing the -O··H_2O structures (Figure 3f) and their shorter hydrogen bonds (blue line in Figure 5b). This enhanced surface interaction weakens the mobility of water molecules. The formation of -OH··OH_2 structures, along with much shorter hydrogen bond lengths (green line in Figure 5b) compared with that in the -O··H_2O structure, leads to the further reduction in the diffusion coefficient for oversaturation systems.

Figure 5c shows the sum percentage of the -O··H_2O and -OH··OH_2 structure and their average surface hydrogen bond lengths between these water structure and the MXene surface. More water molecules are incorporated into -O··H_2O and -OH··OH_2 structures as the initial proton concentration increases. In other words, more and more water molecules are hydrogen bonded with the MXene surface instead of being free to exist in the water layer, suggesting the increasingly important role of the surface hydrogen bond lengths on the diffusion coefficient. Therefore, the variation of the average surface hydrogen bond lengths with proton concentration (black line in Figure 5c) have a trend highly consistent with that for oxygen diffusion coefficient (Figure 5a) from 15% H to 80% H, indicating that the average surface hydrogen bond lengths could serve as a good descriptor to represent the change in the water mobility for the saturation and oversaturation systems. The shorter the average surface hydrogen bond lengths, the lower the water diffusivity. It is worth noting that for 80% H system, the average surface hydrogen bond lengths are slightly longer than 40% H system due to its longer hydrogen bond lengths in the -OH··OH_2 structure (green line in Figure 5b) caused by a higher water coverage on the MXene surface. But for the 80% H system, almost all water molecules are hydrogen-bonded with the MXene surface, and the 40% H system still has a certain amount of the free water (about 15%). Therefore, compared with the 40% H system, the 80% H system has almost no positive contributions of the free water to the diffusion coefficient. As a result, its diffusion

coefficient is still lower than that in the 40% H system even with a little longer average surface hydrogen bond.

These results indicate that the decrease in the mobility of water molecules in saturation and oversaturation stage is all essentially due to the enhanced surface interaction between MXene and water layer.

Discussion. Using V_2CT_x as an example, we have elucidated the detailed dynamic behaviors of the monolayer nanoconfined water in MXene sheets. If there are no protons in the system, strenuous water molecules will spontaneously attack the MXene surface, resulting in the formation of tetrahedron-shaped transition metal oxides. The oxidation rate decreases with the increase of the initial proton concentrations because the solvated Eigen and Zundel cations change the water molecule orientation, thus inhibiting the oxidation rate.

We further found that when more protons are added to the already oxidized system, a reduction reaction begins to occur, as shown in Figure S11. In this case, the top O atom of the oxide is reduced to water by the synergistic effect of the adjacent hydrated protons and the bottom hydroxylated oxygen atoms and then the protruded vanadium atom returns to the original position. The amount of vanadium oxides decreases over time under 150%, 180%, 210%, and 240% proton concentrations (Figure S11). The result is in line with the experimental reports that the oxidation degree of the oxidized $Ti_3C_2T_x$ films could be reduced by hydrogen annealing.[15]

Considering that alkali metals in the main group as same as H element also have positive charges in hydration environments, we supplemented the data of V_2CT_x-H_2O-Li/Na/K systems on the original dataset, and trained NNPs capable of describing the dynamics of Li/Na/K ions in MXene aqueous system. And then 100 ps NPT MD simulations at 300 K and 1 bar were conducted for $V_{2400}C_{1200}O_{2400}$-1000H_2O systems with 0% Li/Na/K, 1% Li/Na/K, 5% Li/Na/K, 10% Li/Na/K. As shown in Figure S12, the amount of vanadium oxides decreases with the increase of Li/Na/K concentrations in range of 0%-10%, which is consistent with the experimental results. [16] Therefore, we conclude that using solvent cations (not just H^+, Li^+, Na^+, K^+) to attract water molecules is a universal strategy to inhibit the MXene oxidation and extend the preservation time. In fact, this is not only applicable to MXenes, but also to all materials that suffer from water-induced oxidation.

Under a specific proton concentration, monolayer water confined in MXene sheets could spontaneous assembly into a 2D hexagonal ice phase, which is also similar with the self-assembly of D_2O observed in previous experiments after doping D^+ ion at 120 K. [1c]. To prove the reliability of this results, we performed ab initio MD (AIMD) simulation at 300 K based on a large model, $V_{96}C_{48}O_{96}$-40H_2O-6H system with the 15% proton content. The simulation results show that a hexagonal ice phase could indeed be formed (Figure S13). For the ice phase, the hydrated protons and surface hydrogen bonds, reducing the movement capacity of the original liquid water, are important for maintaining stability of the hexagonal ice phase at 300 K rather than at extremely low temperature, like the monolayer hexagonal ice phase formed in graphene sheets below 200 K. [4b, 4c]

Notably, there gradually appears some water holes during the transition from the hexagonal ice phase to the amorphous phase (Figure 3b-3d). Figure S14 shows the top view of the amorphous phase in the oversaturation systems. It is worth noting that some rhombic or trigonal water structures are identified on the MXene surface. The similar atomic arrangement (yellow line in Figure S14) illustrates that the positions of these water molecules are strongly affected by the MXene surface lattice due to the strong interaction between the water molecules and the MXene surface. This part of the rhombic or trigonal areas has a much higher density than the hexagonal water area, thus resulting in a lower density of water for the other area (green shading in the Figure S14). We may attribute this to the appearance of water holes and the nature of transition from the ice hexagonal phase to the amorphous phase with an increasing proton concentration. The rhombic or trigonal water usually formed under pressure of up to several or even ten gigapascal [4b, 4c], beyond the ability of the developed NNP at the standard atmospheric pressure. Nevertheless, the formation of such structures also shows the intense hydrogen bond interaction between MXene surface and water molecules. This result also suggests the possibility of more ice phases between the MXenes layers after considering the more extreme water density and a wider range of pressure and temperature conditions.

In addition, we observed the surprising the total depletion of protons in the water layer for 80% H systems. This is because the formation of the -OH··OH_2 structure cause O atoms in water molecule of this structure attaching to the V_2CT_x surface (Figure 3f) rather than participating in the formation of hydrated protons. Therefore, the more hydroxyl groups there are, the more water molecules are occupied by -OH··OH_2 structure, and the less capacity there is to hold protons in the water layer, ultimately resulting in the phenomenon. Further, we confirmed that the similar proton transfer and hydroxylation are also presented in $Ti_3C_2T_x$ through the AIMD simulations on $Ti_3C_2T_x$ systems containing monolayer water and different proton content from 10% H to 80% H. As shown in Figure S15, the ratio of hydroxyl group and hydrated proton for $Ti_3C_2T_x$ have similar evolutionary trend with V_2CT_x, which reveals that the relevant results obtained in this work can be qualitatively extended to other MXenes. We also introduced the equivalent molar concentration of H_2SO_4, HCl and HF for characterize the hydrated proton content in the system, as shown in Table S3. It can be seen that the hydrated protons content presented in our model can be easily achieved experimentally, [14b] facilitating comparison with experimental works.

For saturation and oversaturation systems, the diffusivity of nanoconfined water steadily declines, reaching its lowest value in the system with 50% H. The abundant water molecules strongly hydrogen-bonded with the MXene surface, thus reducing the surface activity and hampering ion insertion and transport process. This is why the MXene with high -OH groups ratio shows poor performance in various energy-related applications.[17] Therefore, it should be noted, when designing MXene-based energy materials, special attention should be paid to the surface groups in MXene sheets and pH value of the environments.

It should be noted that this work mainly focused on the relevant properties of nanoconfined water in V_2CT_x sheets. Given the same oxidation mechanism in nanoconfined water and bulk water systems, the proton effect on the MXene oxidation and the proposed antioxidant strategy are also applicable to the bulk water-MXene interface. But other phenomena driven by the proton concentration and the hydrophilic surface, such as the

identified hexagonal ice phase and the reduction of water diffusivity, may only apply to the nanoconfined water systems. In addition, the surface effects of MXenes remain still quite complex because the surface groups are not limited to -O/-OH groups. For example, it has been reported that utilizing new synthesis methods such as the Lewis acidic and molten salts could modify the MXene surface with high coverage of halogen groups. [18] Different termination may result in different surface effects and proton dynamics. Developing large atomic models [19] covering the MXene family will bring new prospects to further clarify these issues and solve more practical problems through describing the universal characteristics of MXene with complex surface groups in various solvent environments. Finally, the nuclear quantum effects are particularly important in systems involving water. [20] Coupling machine learning potential with path-integral MD simulation [21] [4d] will also provide hopeful prospects for understanding the complete proton-driven dynamic behaviors in MXenes.

Conclusion

Here, we have elucidated the proton-driven dynamic behaviors of monolayer water confined between V_2CT_x sheets utilizing MD simulation based on the NNP and explored the microscopic mechanisms underlying MXene oxidation regulated by protons, the formation of the hexagonal ice phase at room temperature, and the reduction of oxygen diffusion coefficient caused by the water molecule strongly bound to the surface. These unusual behaviors all could be attributed to the water interaction with hydrophilic surfaces and the proton effect, offering valuable insights for the practical applications of MXenes across various fields such as developing antioxidant strategies, identifying novel 2D water phases and optimizing energy storage and conversion.

Acknowledgements

This work was supported by the National Natural Science Foundation of China (Grant No. 12022408 and Grant No. T2325013) and the Department of Science and Technology of Jilin Province of China (Grant No. 20220402016GH). J.-Z.W. acknowledges the financial support by the National Science Foundation's Harnessing the Data Revolution (HDR) Big Ideas Program (Grant No. NSF 1940118). All DFT calculations were carried out at the High-Performance Computing Center of Jilin University, China. The NNPs training and MD simulation were performed on two NVIDIA A100 cards at the National Supercomputer Center in Tianjin, China.

Keywords: MXenes • Nanoconfined Water • Deep Neural Networks • Proton Effect • Hydrophilic Surface

References:

[1] a) R. Z. Ma, D. Y. Cao, C. Q. Zhu, Y. Tian, J. B. Peng, J. Guo, J. Chen, X. Z. Li, J. S. Francisco, X. C. Zeng, L. M. Xu, E. G. Wang, Y. Jiang, *Nature* **2020**, *577*, 60-+; b) C. Lin, N. Avidor, G. Corem, O. Godsi, G. Alexandrowicz, G. R. Darling, A. Hodgson, *Physical Review Letters* **2018**, *120*, 076101; c) Y. Tian, J. N. Hong, D. Y. Cao, S. F. You, Y. Z. Song, B. W. Cheng, Z. C. Wang, D. Guan, X. M. Liu, Z. P. Zhao, X. Z. Li, L. M. Xu, J. Guo, J. Chen, E. G. Wang, Y. Jiang, *Science* **2022**, *377*, 315-319; d) P. Yang, C. Zhang, W. Y. Sun, J. Dong, D. Y. Cao, J. Guo, Y. Jiang, *Physical Review Letters* **2022**, *129*, 046001; e) Q. Dong, Y. Huang, J. Wan, Z. Lu, Z. Wang, C. Gu, J. Duan, J. Bai, *Journal of the American Chemical Society* **2023**, *145*, 8043-8051.

[2] a) T. J. Sun, F. H. Lin, R. L. Campbell, J. S. Allingham, P. L. Davies, *Science* **2014**, *343*, 795-798; b) B. L. Dargaville, D. W. Hutmacher, *Nature Communications* **2022**, *13*, 4222.

[3] a) G. Algara-Siller, O. Lehtinen, F. C. Wang, R. R. Nair, U. Kaiser, H. A. Wu, A. K. Geim, I. V. Grigorieva, *Nature* **2015**, *519*, 443-+; b) L. Fumagalli, A. Esfandiar, R. Fabregas, S. Hu, P. Ares, A. Janardanan, Q. Yang, B. Radha, T. Taniguchi, K. Watanabe, G. Gomila, K. S. Novoselov, A. K. Geim, *Science* **2018**, *360*, 1339-+; c) P. Bampoulis, K. Sotthewes, E. Dollekamp, B. Poelsema, *Surface Science Reports* **2018**, *73*, 233-264; d) K. Gopinadhan, S. Hu, A. Esfandiar, M. Lozada-Hidalgo, F. C. Wang, Q. Yang, A. V. Tyurnina, A. Keerthi, B. Radha, A. K. Geim, *Science* **2019**, *363*, 145-147.

[4] a) J. Jiang, Y. R. Gao, W. D. Zhu, Y. Liu, C. Q. Zhu, J. S. Francisco, X. C. Zeng, *Journal of the American Chemical Society* **2021**, *143*, 8177-8183; b) B. Lin, J. Jiang, X. C. Zeng, L. Li, *Nature Communications* **2023**, *14*, 4110; c) V. Kapil, C. Schran, A. Zen, J. Chen, C. J. Pickard, A. Michaelides, *Nature* **2022**, *609*, 512-+; d) J. Jiang, Y. R. Gao, L. Li, Y. Liu, W. D. Zhu, C. Q. Zhu, J. S. Francisco, X. C. Zeng, *Nature Physics* **2024**, *20*, 456–464.

[5] a) K. Thürmer, S. Nie, *Proceedings of the National Academy of Sciences of the United States of America* **2013**, *110*, 11757-11762; b) S. Maier, B. A. J. Lechner, G. A. Somorjai, M. Salmeron, *Journal of the American Chemical Society* **2016**, *138*, 3145-3151; c) D. Shin, J. Hwang, W. Jhe, *Nature Communications* **2019**, *10*, 286.

[6] a) M. Naguib, M. Kurtoglu, V. Presser, J. Lu, J. J. Niu, M. Heon, L. Hultman, Y. Gogotsi, M. W. Barsoum, *Advanced Materials* **2011**, *23*, 4248-4253; b) M. Naguib, O. Mashtalir, J. Carle, V. Presser, J. Lu, L. Hultman, Y. Gogotsi, M. W. Barsoum, *Acs Nano* **2012**, *6*, 1322-1331; c) F. Wang, F. Tian, X. Xia, Z. Pang, S. Wang, X. Yu, G. Li, Y. Zhao, Q. Xu, S. Hu, L. Ji, X. Zou, X. Lu, *Angewandte Chemie International Edition* **2024**, *63*, e202405315.

[7] A. V. Mohammadi, J. Rosen, Y. Gogotsi, *Science* **2021**, *372*, abf1581.

[8] a) X. L. Li, Z. D. Huang, C. E. Shuck, G. J. Liang, Y. Gogotsi, C. Y. Zhi, *Nature Reviews Chemistry* **2022**, *6*, 389-404; b) Y. Z. Wang, T. C. Guo, Z. N. Tian, K. Bibi, Y. Z. Zhang, H. N. Alshareef, *Advanced Materials* **2022**, *34*, 2108560; c) C. Zheng, Y. Yao, X. H. Rui, Y. Z. Feng, D. Yang, H. G. Pan, Y. Yu, *Advanced Materials* **2022**, *34*, 2204988.

[9] L. Liu, E. Raymundo-Piñero, S. Sunny, P.-L. Taberna, P. Simon, *Angewandte Chemie International Edition* **2024**, *63*, e202319238.

[10] A. Sugahara, Y. Ando, S. Kajiyama, K. Yazawa, K. Gotoh, M. Otani, M. Okubo, A. Yamada, *Nature Communications* **2019**, *10*, 850.

[11] P. F. Hou, Y. M. Tian, Y. Xie, F. Du, G. Chen, A. Vojvodic, J. Z. Wu, X. Meng, *Angewandte Chemie-International Edition* **2023**, *62*, e202304205.

[12] a) Y. Y. L. Sun, C. Zhan, P. R. C. Kent, M. Naguib, Y. Gogotsi, D. E. Jiang, *Acs Applied Materials & Interfaces* **2020**, *12*, 763-770; b) M. Lounasvuori, Y. Y. L. Sun, T. S. Mathis, L. Puskar, U. Schade, D. E. Jiang, Y. Gogotsi, T. Petit, *Nature Communications* **2023**, *14*, 1322; c) J. L. Huang, M. Feng, Y. Peng, C. R. Huang, X. Yue, S. M. Huang, *Small* **2023**, *19*, 202206098; d) M. Shi, R. Wang, L. Li, N. Chen, P. Xiao, C. Yan, X. Yan, *Advanced Functional Materials* **2023**, *33*, 2209777; e) X. Y. Li, T. Wang, Y. C. Cai, Z. D. Meng, J. W. Nan, J. Y. Ye, J. Yi, D. P. Zhan, N. Tian, Z. Y. Zhou, S. G. Sun, *Angewandte Chemie-International Edition* **2023**, *135*, e202218669.

[13] a) H. Wang, L. F. Zhang, J. Q. Han, W. N. E, *Computer Physics Communications* **2018**, *228*, 178-184; b) Y. Z. Zhang, H. D. Wang, W. J. Chen, J. Z. Zeng, L. F. Zhang, H. Wang, W. E, *Computer Physics Communications* **2020**, *253*, 107206.

[14] a) S. Kumar, *Small* **2024**, *20*, 2308225; b) Y. Wei, P. Zhang, R. A. Soomro, Q. Zhu, B. Xu, *Advanced Materials* **2021**, *33*, 2103148.

[15] Y. Lee, S. J. Kim, Y. J. Kim, Y. Lim, Y. Chae, B. J. Lee, Y. T. Kim, H. Han, Y. Gogotsi, C. W. Ahn, *Journal of Materials Chemistry A* **2020**, *8*, 573-581.

[16] a) M. Lounasvuori, T. Zhang, Y. Gogotsi, T. Petit, *The Journal of Physical Chemistry C* **2024**, *128*, 2803-2813; b) A. VahidMohammadi, M. Mojtabavi, N. M. Caffrey, M. Wanunu, M. Beidaghi, *Advanced Materials* **2019**, *31*, 1806931; c) X. Y. Wang, Z. Y. Wang, J. S. Qiu, *Angewandte Chemie-International Edition* **2021**, *60*, 26587-26591.

[17] a) H. H. Shi, P. P. Zhang, Z. C. Liu, S. Park, M. R. Lohe, Y. P. Wu, A. S. Nia, S. Yang, X. L. Feng, *Angewandte Chemie-International Edition* **2021**, *60*, 8689-8693; b) Y. A. Jiang, T. Sun, X. Xie, W. Jiang, J. Li, B. B. Tian, C. L. Su, *Chemsuschem* **2019**, *12*, 1368-1373; c) J. Li, X. T. Yuan, C. Lin, Y. Q. Yang, L. Xu, X. Du, J. L. Xie, J. H. Lin, J. L. Sun, *Advanced Energy Materials* **2017**, *7*, 1602725; d) C. Eames, M. S. Islam, *Journal of the American Chemical Society* **2014**, *136*, 16270-16276.

[18] a) Y. Li, H. Shao, Z. Lin, J. Lu, L. Liu, B. Duployer, P. O. Å. Persson, P. Eklund, L. Hultman, M. Li, K. Chen, X.-H. Zha, S. Du, P. Rozier, Z. Chai, E. Raymundo-Piñero, P.-L. Taberna, P. Simon, Q. Huang, *Nature Materials* **2020**, *19*, 894-899; b) M. Shen, W. Jiang, K. Liang, S. Zhao, R. Tang, L. Zhang, J.-Q. Wang, *Angewandte Chemie International Edition* **2021**, *60*, 27013-27018.

[19] a) S. Takamoto, D. Okanohara, Q. J. Li, J. Li, *Journal of Materiomics* **2023**, *9*, 447-454; b) D. Zhang, X. Liu, X. Zhang, C. Zhang, C. Cai, H. Bi, Y. Du, X. Qin, J. Huang, B. Li, Y. Shan, J. Zeng, Y. Zhang, S. Liu, Y. Li, J. Chang, X. Wang, S. Zhou, J. Liu, X. Luo, Z. Wang, W. Jiang, J. Wu, Y. Yang, J. Yang, M. Yang, F.-Q. Gong, L. Zhang, M. Shi, F.-Z. Dai, D. M. York, S. Liu, T. Zhu, Z. Zhong, J. Lv, J. Cheng, W. Jia, M. Chen, G. Ke, Weinan, L. Zhang, H. Wang, *Arxiv* **2023**, arXiv:2312.15492.

[20] M. E. Tuckerman, D. Marx, M. Parrinello, *Nature* **2002**, *417*, 925-929.

[21] A. O. Atsango, T. Morawietz, O. Marsalek, T. E. Markland, *The Journal of Chemical Physics* **2023**, *159*, 074101.

Entry for the Table of Contents

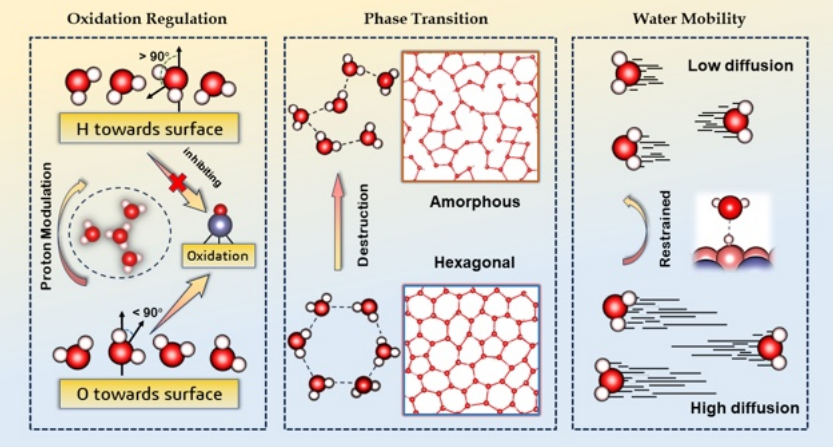

We reported the detailed proton-driven dynamic behaviors of nanoconfined water between hydrophilic MXene sheets using molecular dynamics simulation based on the active learning machine learning potential trained by deep neural network algorithms. These findings have illuminated several novel phenomena including the MXene oxidation rate regulated by protons, the formation of a hexagonal ice phase exhibiting unconventional bonding patterns at room temperature, and a significant reduction in water diffusivity.

Personal Twitter @Xing_Meng_2020